Computer-Aided Design and Applications

http://www.cadanda.com

An Integrated Imaging and BEM for Fast Simulation of Freeform Objects

Xiaolin Chen[1] and Hui Zhang[2]

[1]Washington State University Vancouver, chenx@vancouver.wsu.edu
[2]Washington State University Vancouver, zhang@vancouver.wsu.edu

ABSTRACT

Proposed in this paper is a boundary-type approach as a way to increase efficiency of reverse engineering simulation of complex freeform digital models acquired from scanning. The developed method utilizes surface discretization nature of the boundary element method (BEM), and eliminates time-consuming NURBS surface/solid generation and volume discretization needed in domain-type simulation. Unstructured as-scanned image data is imported and regularized into a well-behaved BEM mesh in the computation. The developed BEM achieves a near $O(N)$ computational complexity, by coupling the conventional BEM (of $O(N^3)$) with the fast multipole acceleration. Numerical examples are presented to demonstrate its effectiveness and efficiency. Preliminary results show that the developed BEM can be a promising tool for many reverse engineering simulation applications involving highly complex organic shapes and large-scale models, e.g., the ones acquired from medical imaging.

Keywords: boundary element, fast multipole, reverse engineering simulation, freeform object.
DOI: 10.3722/cadaps.2008.371-380

1. INTRODUCTION

Digital modeling of existing complex freeform objects has gained lots of attention in recent years [1, 2]. As an alternative to modeling objects with the aid of CAD software, digital modeling allows us to reconstruct geometric models from real or "as-built" objects using non-destructive scanning technology. The acquired digital models are increasingly used in various reverse engineering applications. In the field of industrial design and ergonomics for example, aesthetic and ergonomic freeform designs that are hard to model using standard CAD packages are captured from sculptured prototypes and used in product design phase [3, 4]. Digital models are also heavily used in medical and dental fields to capture the complex geometry of the human body for downstream applications [5, 6].

It is desirable to perform fast and accurate engineering simulation immediately after digital modeling. Efforts towards this end will enable real-time mechanical characterization of scanned complex objects, which may benefit the medical industry, e.g., to develop simulation-based diagnosis or surgery training systems using patient-specific scan models. Many researchers have introduced reconstructed geometries into their standard finite element studies [7, 8]. Some image-based finite element methods were proposed in [9, 10], where bitmap information from scan images could be translated into brick elements for finite element analysis. The image-based methods eliminated time-consuming CAD reconstruction needed for standard FEM and made a significant step forward. Although their lack of smooth and accurate boundary representation in the translated voxel model seems an open issue [11], some research results along this line have demonstrated the usefulness of these methods [12, 13]. Especially, the image-based FEM has gained certain popularity in mechanical property studies of complex bio-structures [14]. As more and more studies rely on realistic computational models reconstructed at different length scales from high-resolution scan images, computational cost has become a serious challenge for finite element studies of these models. Fairly dense volume meshes are needed to correctly represent the geometric intricacies in complex freeform shapes. It was found in a recent FEM study [15] that approximately 6 weeks of wall-clock time were spent to obtain results from a human proximal

femur microstructure bone model with over 96 million brick elements (using thirty processors of an SGI/Cray Origin 2000 with a total of 128 processors and 57 GB memory).

In this paper, we aim to develop a new, computationally efficient solution for fast reverse engineering simulation of complex freeform objects. We propose an integrated imaging and boundary element approach, which exploits the surface discretization nature of BEM and regularizes directly the scan image data into a BEM mesh. To speed up computation for large-scale problems, fast multipole method (FMM) is implemented to accelerate the conventional BEM. The developed BEM is compared with the standard FEM in reverse engineering simulation through numerical studies. Our paper is organized as follows: Section 2 introduces the boundary-type computational scheme in comparison with the domain-type scheme for reverse engineering simulation. Section 3 presents some important formulation for the conventional BEM and the fast multipole acceleration, taking 3D steady-state heat conduction analysis as an example. Section 4 gives a case study on a thermal analysis of a laser scanned digital freeform model, first by the FEM with a commercial package and then by the in-house developed BEM. A second example of an x-ray scanned trabecular bone microstructure study is then presented using the developed BEM to demonstrate its effectiveness and efficiency for large scale problems. Results are finally discussed and concluded.

2. DOMAIN AND BOUNDARY COMPUTATION FOR REVERSE ENGINEERING SIMULATION

The life cycle of reverse engineering simulation is categorized into two major steps: imaging and computation. During imaging, a physical object is converted into a digital representation. A digitizer collects geometric coordinates on the object's surface into a 3D point cloud. After removing erroneous points (i.e., outliers caused by the influence of surface reflectance in laser scanning), a tessellated surface (polygon mesh) can be created from the point cloud through surface triangulation. The end product of the imaging process is in general a polygon surface of the scanned object stored in stereolithography (STL) format.

After imaging, domain-type or boundary-type numerical computation can be employed to analyze the digital model. The domain computation represented by the FEM has been predominantly used for engineering analysis. When applied for reverse engineering simulation, domain computation presents an inefficient workflow (See Fig. 1(a)). A solid model, e.g. represented using non-uniform rational B-spline (NURBS) functions, needs to be reconstructed from the surface scan data to bridge the gap between imaging and computation. The complexity of the data transformation involved often necessitates the use of sophisticated reverse engineering software together with lots of user intervention. Computation relies heavily on successful CAD reconstruction. For objects with complex organic shapes, the modeling accuracy can be easily impaired. The solid reconstruction can also be very difficult and sometimes even become impossible.

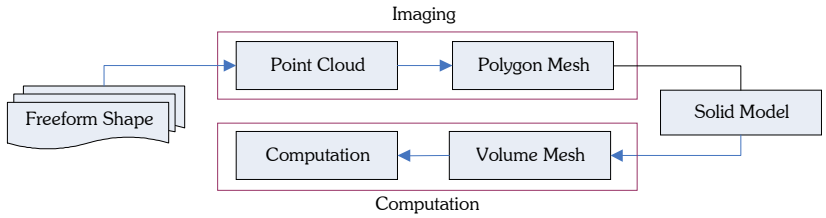

(a) a traditional domain-type computational scheme

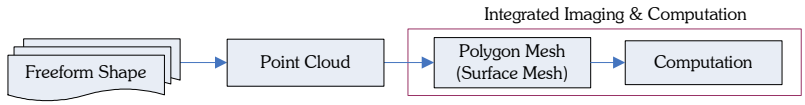

(b) a new boundary-type computational scheme

Fig. 1: Domain- and boundary-type reverse engineering simulation.

To remove the computation dependency on solid model reconstruction, we point out a new workflow that is realized through the boundary-type computation. As shown in Fig. 1(b), the proposed approach is a lean process, in which imaging and computation are tightly integrated by direct translation of polygon surface scan into mesh discretization for the BEM. As a representative boundary-type approach, BEM has been known for decades for its advantage in the modeling stage. A major stumbling block in this method is its slow solution time, which has been preventing it from being widely used for many practical and computationally demanding problems. Recently, some studies [16, 17, 18] have shown that the BEM can be combined with the fast multipole method to greatly accelerate its

computation. A computational cost of $O(N^3)$ for solving system equations in conventional BEM can be reduced to $O(N)$ in FMM-accelerated BEM, with N being the problem size. The BEM together with the FMM acceleration may offer the boundary-type computation a great advantage in many interesting reverse engineering simulation applications.

3. BEM WITH FAST MULTIPOLE ACCELERATION FOR 3D STEADY-STATE HEAT CONDUCTION

In this section, we follow the classic works in [19] for describing the BEM formation, taking 3D steady-state heat conduction as an example. More details on the BEM development for various kinds of engineering simulation can also be readily found in [19, 20]. In BEM, the governing partial differential equations are transformed into integral representation referred to as the boundary integral equations (BIEs). The problem is then solved based on the discretized BIEs over a domain's boundary. The problem dimension is generally reduced by one in BEM. In other words, only surface discretization is needed for 3D problems. Also the governing equations are exactly satisfied at each field point so that it can provide more accurate solutions even by using a fairly coarse boundary mesh [21].

For 3D steady-state heat conduction, assuming no internal heat source, the temperature potential field ϕ has to satisfy the following Laplace equation [19]:

$$\nabla^2\phi = 0 \tag{1}$$

To establish the BIEs, we consider the Green's function (also referred to as the fundamental solution) at a field point *y* in an infinite medium due to a unit heat source at point *x*. The Green's function satisfies the following equation:

$$\nabla^2 G(x,y) + \delta(x,y) = 0 \tag{2}$$

,where $\delta(x,y)$ is the Dirac δ-function. $G(x,y)$ is the Green's function given by $G(x,y) = \frac{1}{4\pi r}$ for a 3D potential problem, with *r* representing the distance between the source point *x* and the field point *y*.

Applying the Gauss theorem, we obtain the following identity (or a reciprocal relation) involving the potential field ϕ and the fundamental solution:

$$\int_V [G(x,y)\nabla^2\phi(y) - \phi(y)\nabla^2 G(x,y)]dV = \int_S [G(x,y)\frac{\partial\phi(y)}{\partial n(y)} - \phi(y)\frac{\partial G(x,y)}{\partial n(y)}]dS(y) \tag{3}$$

,where n(y) is the surface normal at a field point *y*.

Substituting equations (1) and (2) into (3), we derive an integral representation for the potential field:

$$\phi(x) = \int_S \left[G(x,y)\frac{\partial\phi(y)}{\partial n(y)} - \phi(y)\frac{\partial G(x,y)}{\partial n(y)} \right] dS(y), \forall x \in V \tag{4}$$

Here *x* is an arbitrary source point inside domain *V* and *y* an arbitrary field point on the domain's boundary *S*. A domain potential is thus related to some integral of surface potentials and surface fluxes through equation (4).

Now define heat flux q as $q(y) = \frac{\partial\phi(y)}{\partial n(y)}$ and introduce $F(x,y) = \frac{\partial G(x,y)}{\partial n(y)} = -\frac{1}{4\pi r^2}\frac{\partial r}{\partial n(y)}$. Let the source point *x* in a domain *V* approach the boundary *S*, we will have the following boundary integral equation (BIE):

$$c(x)\phi(x) = \int_S [G(x,y)q(y) - F(x,y)\phi(y)]dS(y), \forall x \in S \tag{5}$$

, where *c(x)* is a constant coefficient depending on the smoothness of the boundary at a point *x* (e.g., $=\frac{1}{2}$, for smooth surface), Notice that both the source point *x* and the field point *y* are located on the boundary surface *S* now.

To subtract the kernel singularity existing in the BIE, apply a special loading case with constant $\phi(y)$ and zero $q(y)$ (similar to a rigid body motion for elasticity) to Equation (5), and the coefficient term can be expressed as [22]:

$$c(x) = -\int_S F(x,y)\,dS(y), \forall x \in S \tag{6}$$

Substituting Equation (6) into (5), we derive the following form of BIE:

$$\int_S F(x,y)\big[\phi(y)-\phi(x)\big]dS(y)=\int_S G(x,y)q(y)\,dS(y)\,,\ \forall x\in S \tag{7}$$

Eq. (7) is a non-singular BIE form. The singularity in *G* kernel can be eliminated by using polar coordinate transformation ($ds=rdrd\theta$), and the singularity in *F* kernel can also be removed after using one-term Taylor's series expansion of the density function (temperature ϕ) together with the polar coordinate transformation.

After discretizing the boundary *S* into elements with nodes, we can write the BIE at each node. Applying the boundary conditions and constraints, the BIEs can be rearranged into a linear equation system [19]:

$$\mathbf{Az}=\mathbf{b} \tag{8}$$

where **A** is the coefficient matrix, **b** is the known load vector and **z** the unknown vector.

The coefficient matrix **A** represents the thermal interaction between any two node points. The final linear system of equations collected from all surface nodes is then solved simultaneous to obtain the unknown temperatures or heat fluxes on the boundary. Although BEM relies solely on the surface discretization, accurate information in the interior domain can be readily obtained from equation (4), once the surface information is obtained from equation (8).

In the BIEs, matrix **A** is dense and non-symmetrical. Thus, the conventional BEM approach can only handle small BEM models with a few thousands of nodes on a desktop PC, due to the computing cost that is $O(N^2)$ for computing matrix **A** (Because, for x at every node, integrations need to be done over all the other elements/nodes) and $O(N^3)$ for solving the system of equations with direct solvers.

To accelerate the BEM solution, we use the fast multipole method [16, 17], which is demonstrated to be a promising approach to accelerate the solution of large-scale problems. Using the FMM with the BEM, near $O(N)$ computational efficiencies of the BEM can be achieved. Some basic formulas related to the FMBEM are presented next. Introduce the following expansion for the key term in the Green's kernel function [18]:

$$\frac{1}{r}=\frac{1}{r(x,y)}=\sum_{n=0}^{\infty}\sum_{m=-n}^{n}\overline{S_{n,m}}(\overrightarrow{Ox})R_{n,m}(\overrightarrow{Oy}) \tag{9}$$

where r is the distance between source point x and field point y. $\left|\overrightarrow{\mathbf{Oy}}\right|<\left|\overrightarrow{\mathbf{Ox}}\right|$, with O representing an expansion point close to the field y, $S_{n,m}$ and $R_{n,m}$ are solid harmonic functions, and $\overline{(\ )}$ means the complex conjugate.

The fundamental solutions for the G and F kernel become the following series of expansion [18]:

$$G(\mathbf{x},\mathbf{y})\approx\frac{1}{4\pi}\sum_{n=0}^{p}\sum_{m=-n}^{n}\left[\overline{S_{n,m}}(\overrightarrow{Ox})R_{n,m}(\overrightarrow{Oy})\right] \tag{10}$$

$$F(\mathbf{x},\mathbf{y})=\frac{\partial G(x,y)}{\partial n(y)}\approx\frac{1}{4\pi}\sum_{n=0}^{p}\sum_{m=-n}^{n}\left[\overline{S_{n,m}}(\overrightarrow{Ox})\frac{\partial R_{n,m}(\overrightarrow{Oy})}{\partial n(y)}\right] \tag{11}$$

The significance of expression (9) is that the kernel $G(\mathbf{x},\mathbf{y})$ is now a sum of functions, in which the source point x and field point y are separated by introducing the third point O. This expression enables one to evaluate the integrals in the BIEs only once, and thus reduce the computation significantly. To see this, consider the integral in BIE on a sub-domain S_c of *S* away from the source point x. Applying expression (10) and (11), with point O being close to sub-domain S_c , we obtain:

$$\int_{S_c} G(x,y)q(y)\,dS(y)\approx\frac{1}{4\pi}\sum_{n=0}^{p}\sum_{m=-n}^{n}\left[\overline{S_{n,m}}(\overrightarrow{Ox})M_{n,m}(O)\right] \tag{12}$$

$$\int_{S_c} F(x,y)\phi(y)\,dS(y)\approx\frac{1}{4\pi}\sum_{n=0}^{p}\sum_{m=-n}^{n}\left[\overline{S_{n,m}}(\overrightarrow{Ox})\tilde{M}_{n,m}(O)\right] \tag{13}$$

in which $M_{n,m}$ and $\tilde{M}_{n,m}$ are called multipole moments centered at point *O* and given by:

$$M_{n,m}(O)=\int_{S_c} R_{n,m}(\overrightarrow{Oy})q(y)\,dS(y) \tag{14}$$

$$\tilde{M}_{n,m}(O) = \int_{S_c} \frac{\partial R_{n,m}(\overrightarrow{Oy})}{\partial n(y)} \phi(y)\, dS(y) \tag{15}$$

Evaluations of these two moments are independent of the source point and thus need to be calculated only once. With these expansions and translations, an order N efficiency in computing can be achieved [16, 17].

4. RESULTS

4.1 Reverse Engineering Simulation by FEM – The Oil Lamp Example

As the first example, an oil lamp (Fig. 2(a)) was digitized using a Konica Minolta VIVID 910 laser scanner for reverse engineering comparison study. Range scan images (see Fig. 2(b)) were collected to describe the object from different views. A 3D point cloud (see Fig. 2(c)) was formed by registering range images into one common coordinate system. After removing the noise defects, a digital model of polygon surface (see Fig. 2(d)) was developed.

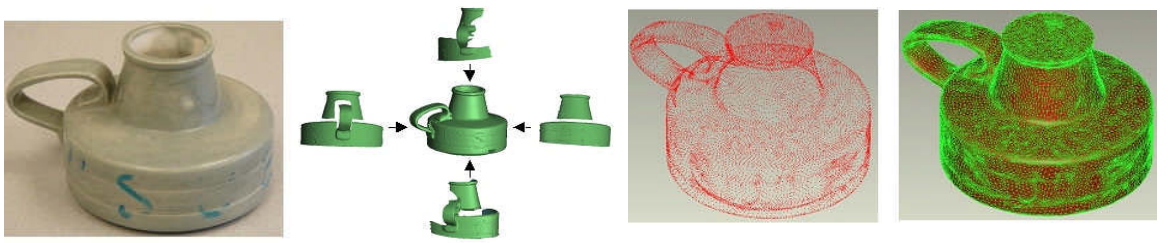

(a) physical object (b) range scan image registration (c) point cloud data (d) polygon surface

Fig. 2: Digital model acquisition of a freeform shape - an oil lamp example.

Preprocessing of the digital model for FEM study was performed using commercial reverse engineering software Geomagic Studio, with which a NURBS surface (see Fig. 3(a)) and a solid CAD model (see Fig. 3(b)) were generated and imported into commercial FEM package ANSYS. After meshing the volume with tetrahedral elements (see Fig. 3(c)), converged temperature distribution (see Fig. 3(d)) was obtained in ANSYS. For this steady-state thermal study, the average edge length of tetrahedral elements was set to be close to that of triangular elements in the polygon mesh. The base material was assumed to have a constant thermal conductivity of 1 W/m· □C. The bottom and top surface temperature were fixed at a value of 0□ and 1□C, respectively.

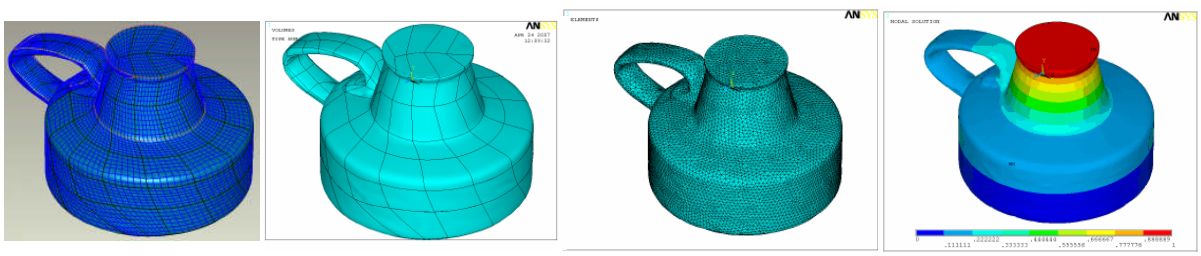

(a) NURBS surface (b) solid model (c) volume mesh (d) FEM temperature results

Fig. 3: Major steps in a traditional finite element scheme.

4.2 Reverse Engineering Simulation by the Developed BEM – The Oil Lamp Example

Next, the digital model was simulated with the developed BEM. To make sure the scanned image data translate into high-quality BEM surface mesh, mesh regularization was implemented to facilitate the BEM computation. A simple radius-ratio element shape measure was adopted in this study. With this measure, ill-shaped elements that may affect the convergence and computational accuracy were singled out and treated accordingly. For instance, a cap-like element with a very large angle would be regularized by edge swapping. A needle-like element would be removed by collapsing the degenerating edge into a vertex.

The polygon surface shown in Fig 2(d) was taken as the input for mesh regularization. The radius-ratio measure used the ratio between the diameter of the inscribed circle and the radius of the circumscribed circle as the element quality factor (Q). By this definition, all Q factors fell in the range between 0 and 1, with higher Q indicating a better element shape. A control factor of 0.3 was specified in the regularization procedure. Elements with Q factors lower than the control factor were regularized. Fig. 4 shows the mesh improvement, in which the Q factor distributions were represented by a solid blue line and a dashed read line before and after regularization, respectively. As shown in Fig. 4, after regularization, number of elements with Q factors lower than 0.3 was significantly reduced, and those with Q in between 0.6 and 1 were greatly increased.

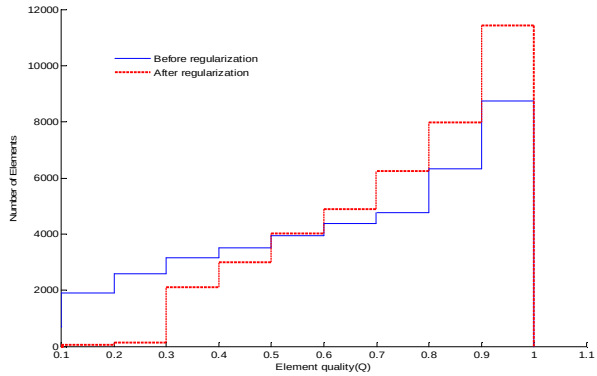

Fig. 4: Element quality (Q) factor distribution before and after regularization.

The regularized BEM mesh was plotted in Tecplot in Fig. 5(a). The same material property and boundary conditions were applied as in the FEM case. Results obtained from the developed BEM were shown in Fig. 5(b), which compares very well with the ANSYS results in Fig. 3(d).

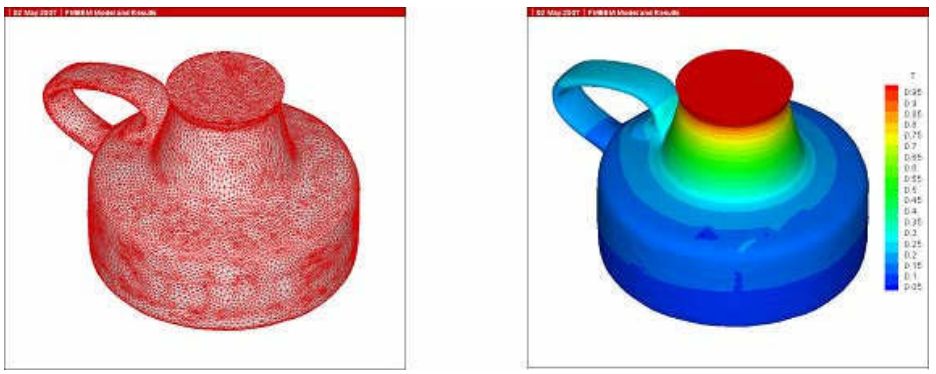

(a) regularized BEM mesh (b) temperature results from the developed BEM

Fig. 5: Major steps in a new BEM scheme.

To quantify the difference between ANSYS and BEM results, surface temperature distributions were summarized using histograms given in Fig. 6, in which ANSYS and BEM results were represented by solid blue and dashed red lines, respectively. The frequency distributions of surface nodes in the temperature range 0^{o} to $1\ ^{o}C$ were plotted using twenty intervals in Fig. 6(a), in which both ANSYS and BEM showed a similar distribution pattern. In Fig. 6(b), mean nodal temperature was plotted with the corresponding node percentage for each interval. Both ANSYS and BEM results showed that nodes with temperature below $0.25\ ^{o}C$ accounted for about 85% of total nodes on the surface. For the remaining 15%, both results showed a steep change in nodal temperatures from 0.25^{o} to $1\ ^{o}C$, which correctly reflected the neck temperature field of oil lamp. The percentage weighted average temperature difference between ANSYS and BEM was calculated based on Fig. 6(b). The global relative error between the two was found to be less than 2.6%. Note that the histogram difference in node distribution/counts did not necessarily indicate a different temperature field prediction from ANSYS and BEM. The non-uniform BEM mesh also contributed substantially to the

difference, e.g., for the interval where BEM node count was comparatively larger than that from ANSYS, it was found that local mesh density was also higher in BEM due to the existence of scattered node clusters in the scan data.

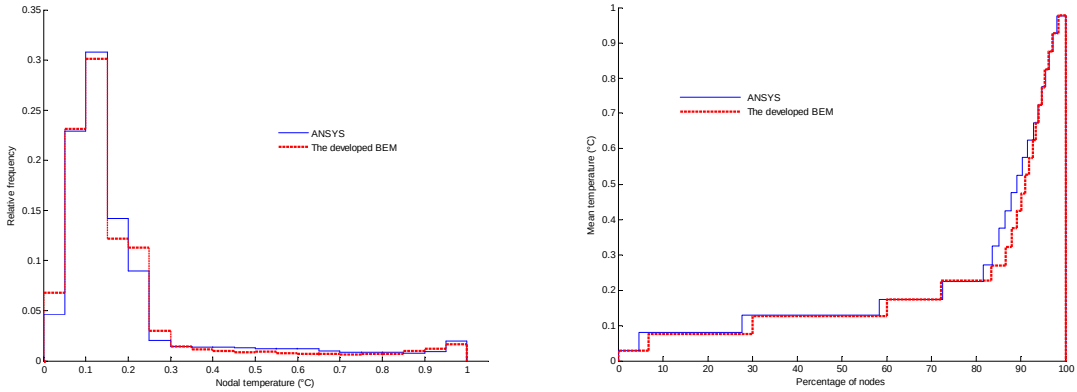

(a) node counts for temperature intervals (b) node distribution with mean temperature

Fig. 6: Histogram comparison of surface temperature results from ANSYS and the developed BEM.

To compare computational performance between the FEM and the developed BEM, both simulations were run on the same desktop PC with a 3.2 GHz Pentium IV processor and 1.5 GB memory. The FEM volume mesh contained 403,271 tetrahedral elements. The BEM mesh consisted of 42,810 triangular elements to maintain a similar surface mesh density as in the volume mesh. The recorded CPU time was close to 1 hour (3593 seconds) for ANSYS, and less than 15 minutes (885 seconds) for the accelerated BEM simulation. As expected, the developed BEM sped up the conventional BEM computation and showed great advantage over the highly optimized commercial code ANSYS by significantly reducing the problem size and complexity, and therefore, the computational cost for such simulation.

Note that the comparison was made without considering the time saved to eliminate NURBS and solid reconstruction steps in the FEM scheme. To perform those tasks alone would easily take hours or even days for inexperienced users as the scan object becomes complex.

As mentioned earlier in section 3, although the BEM relies solely on surface discretization, accurate information in any interior location of interest can be readily obtained after the boundary computation. Compared with the domain scheme, in which detailed computation will be carried out at any cost throughout a discretized volume, the boundary scheme offers more flexibility to allow user retrieval of field (volume) information at interested locations at a later stage when needed. This flexibility is particularly important for applications where the problem size is huge and yet only surface results of the 3D domain is needed to finish a task. A good example of such applications is to perform 'virtual' testing of image-scanned biological tissues, porous materials or other advanced materials to extract their effective mechanical properties.

4.3 Reverse Engineering Simulation by the Developed BEM – The Trabecular Bone Example

As the second sample, thermal analyses of x-ray scanned microstructural bone models were performed using the developed BEM, to evaluate its capability in handling large scale problems with more complex geometry. A SkyScan micro-CT scanner was used for sectional image acquisition of various bovine trabecular microstructure samples. Digital models with true trabecular morphology were then developed by surface reconstruction from the micro-CT scanner.

Surface polygon of the acquired digital models was imported for the fast BEM analysis. Solutions were successfully obtained on a desktop PC (3.2 GHz Pentium IV processor and 1.5 GB memory). Fig. 7 shows the BEM meshes and thermal results for healthy and weak (e.x. osteoporous bone) trabecular microstructures. About 70k and 200k triangular elements were used for the BEM meshes of healthy and weak bones, respectively. The base material was again assigned a constant thermal conductivity of 1 W/m· °C. As shown in Fig. 7, the developed BEM nicely captured the heat flow from one end to the other where both ends were held at constant temperatures of 0°C and 1°C, respectively.

The CPU time consumed by the developed BEM was plotted in Fig. 8 for three different trabecular samples. As shown in Fig. 8, the CPU time increased almost linearly with the problem size for the developed BEM. Roughly 0.6, 1.3 and 3.4 hours were spent on the desk PC to obtain results for the three microstructural models containing about

70k, 120k and 200k triangular elements, respectively. To achieve similar accuracy, a domain analysis, ex., using the FEM, would generally require models with significantly increased problem size (by 10-100 folds) and hence would take much longer solution time. These preliminary results clearly demonstrate the effectiveness of the developed BEM, which could be especially good while not limited for applications where only boundary wall (can be both exterior and interior) information is needed.

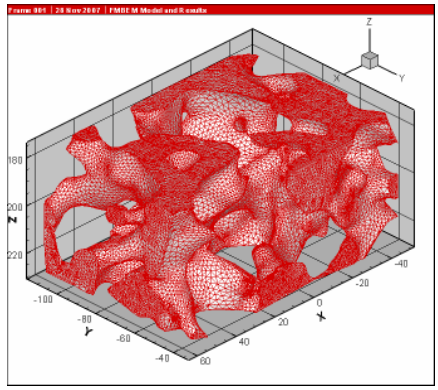

(a) healthy trabecular bone microstructure

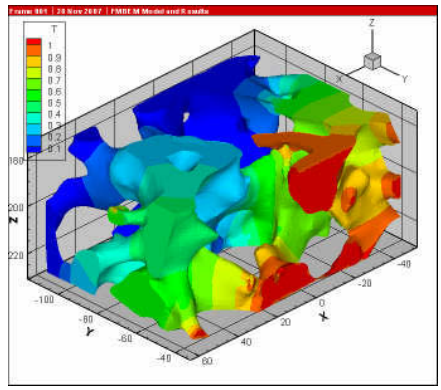

(b) temperature results from the developed BEM

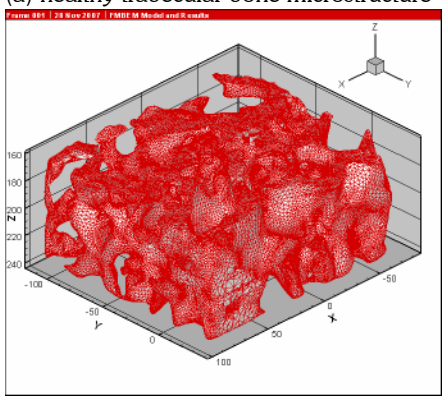

(c) weak trabecular bone microstructure

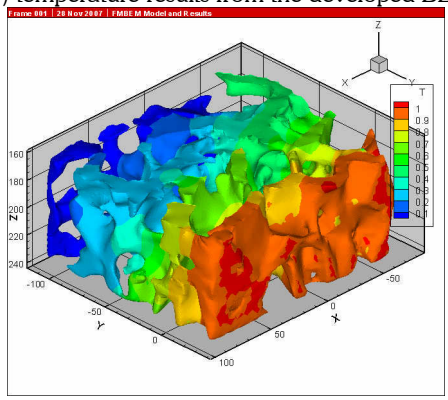

(d) temperature results from the developed BEM

Fig. 7: Trabecular microstructure study for healthy and weak bone samples.

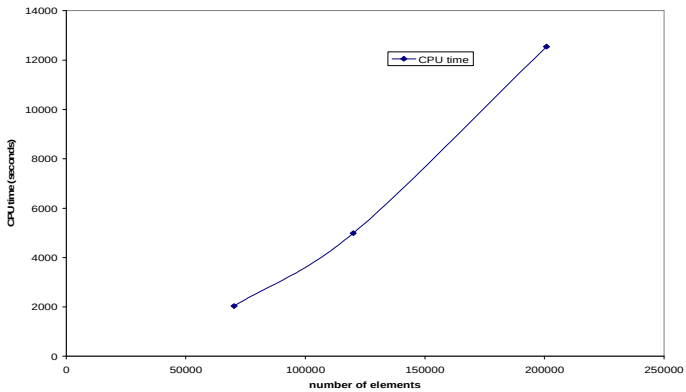

Fig. 8: Linear increase in CPU time with problem size for the developed BEM.

Further implementation of the developed method may consider adding evaluation of secondary variables (heat flux distribution) to study the effective thermal conductivity of these and other types of samples, e.g., porous solder

joints for electronics packaging. Internal heat sources can be included by performing volume-to-surface integral transformation in the BEM formulation. Time history effect (transient thermal) can also be implemented to expand the study for more sophisticated real life problems, e.g. injection mold cooling analysis.

The developed BEM with FMM acceleration, though only presented for steady-state thermal analysis in this study, can be readily extended for elasticity. Multiple material domains with interface effects can also be considered, to tackle problems with heterogeneous material properties. With further development, more interesting numerical experiments can be conducted, e.g. virtual tensile, compressive or bending testing of realistic high-resolution digital objects. Modeling results of these studies can then be used for prediction and characterization, e.g., biomechanical behaviors from patient-specific scan images. Once fully-developed, it can be a promising tool for studies in many areas, including material science, biomedical engineering, and traditional design.

5. CONCLUSIONS

An integrated imaging and fast boundary element method is developed in this paper for reverse engineering simulation of complex freeform objects. The developed BEM allows for direct import of digital scan images for fast boundary computation, and therefore provides a distinctive advantage over the existing domain-type approach, which requires time-consuming solid model reconstruction and discretization. A simple mesh regularization procedure is implemented in this study to facilitate the computation. To accelerate the conventional BEM computation, fast multipole algorithm is implemented in the developed BEM. A numerical comparison study is provided to show the effectiveness of the developed BEM, which achieves similar accuracy and takes only a fraction of the computational time needed by highly optimized commercial code ANSYS. The efficiency of the developed BEM is also demonstrated by a large-scale numerical study involving complex organic shapes, where near-linear increase of the CPU time is achieved with the problem size. Results show that the developed BEM with FMM acceleration can be a competitive alternative for many interesting reverse engineering simulation applications.

6. ACKNOWLEDGEMENT

The authors would like to acknowledge the support by the M. J. Murdock foundation and OGRD at Washington State University Vancouver. The authors also thank the reviewers for their valuable comments about this paper.

7. REFERENCES

[1] Werner, A.; Skalski, K.; Piszczatowski, S.; Swieszkowski, W.; Lechniak, Z.: Reverse engineering of free-form surfaces, Journal of Materials Processing Technology, 76(1-3), 1998, 128-132.

[2] Fabio, R.: From point cloud to surface: the modeling and visualization problem, International Archives of the Photogrammetry, Remote Sensing and Spatial Information Sciences, Vol. XXXIV-5/W10, 2003.

[3] El-Hakim, S.; Whiting, E.; Gonzo, L.; Girardi, S.: 3-D reconstruction of complex architectures from multiple data, 3D Virtual Reconstruction and Visualization of Complex, Italy, 2005.

[4] Bassoli, E.; Gatto, A.; Iuliano, L.; Leali, F.: Design for manufacturing of an ergonomic joystick handgrip, World Automation Congress, 18, 2004, 461-466.

[5] Webb, P. A.: A review of rapid prototyping (RP) techniques in the medical and biomedical sector, Journal of Medical Engineering & Technology, 24(4), 2000, 149-153.

[6] Singare, S.; Dichen, L.; Bingheng, L.; Yanpu, L.; Zhenyu, G.; Yaxiong, L.: Design and fabrication of custom mandible titanium tray based on rapid prototyping, Med Eng Phys., 26(8), 2004, 671-676.

[7] Endo, M.: Reverse Engineering and CAE, JSME International Journal Series C, 48(2), 2005, 218-223.

[8] Argento, M.; Barone, S.; Bianconi, F.; Conti, P.; Rosati, E.: Titolo Reverse engineering and CFD analysis: a case study, International Conference on Applied Simulation and Modelling, Greece, 2004.

[9] Hollister, S. J.; Riemer, B. A.: Digital image based finite element analysis for bone microstructure using conjugate gradient and Gaussian filter techniques, The International Society for Optical Engineering, San Diego, 1993, 95-106.

[10] Langer, S. A.; Fuller, E. R.; Carter, W. C.: An image-based finite element analysis of material microstructures, Computing in science and engineering, 3(3), 2001, 15-23.

[11] Charras, G. T.; Guldberg, R. E.: Improving the local solution accuracy of large-scale digital image-based finite element analyses, Journal of Biomechanics, 33(2), 2000, 255-259.

[12] Kujime, T.; Tane, M.; Hyun, S. K.; Nakajima, H.: Three-dimensional image-based modeling of lotus-type porous carbon steel and simulation of its mechanical behavior by finite element method, Materials Science and Engineering A 460-461, 2007, 220-226.

[13] Anderson, D. E.; Cotton, J. R.: Mechanical analysis of percutaneous sacroplasty using CT image based finite element models, Medical Engineering & Physics 29, 2007, 316-325.
[14] Hollister, S. J.; Kikuchi, N.: Homogenization theory and digital imaging: a basis for studying the mechanics and design principles of bone tissue, Biotechnology and Bioengineering, 43, 1994, 586-596.
[15] Rietbergen, B. V.; Huiskes, R.; Eckstein, F.; Rüegsegger, P.: Trabecular bone tissue strains in the healthy and osteoporotic human femur, Journal of Bone and Mineral Research, 18(10), 2003, 1781-1788.
[16] Nishimura, N.: Fast multipole accelerated boundary integral equation methods, Applied Mechanics Reviews, 55(4), 2002, 299-324.
[17] Liu, Y. J.; Nishimura, N.: The fast multipole boundary element method for potential problems: a tutorial, Engineering Analysis with Boundary Elements, 30(5), 2006, 371-381.
[18] Shen, L.; Liu, Y. J.: An adaptive fast multipole boundary element method for three-dimensional potential problems, Computational Mechanics, 39(6), 2007, 681-691.
[19] Banerjee, P. K.: The Boundary Element Methods in Engineering, McGraw-Hill, Berkshire, England, 1994.
[20] Brebbia, C. A.; Dominguez, J.: Boundary Elements – An Introductory Course, McGraw-Hill, New York, 1989.
[21] Mukherjee, S.; Morjaria, M.: On the efficiency and accuracy of the boundary element method and the finite element method, International Journal for Numerical Methods in Engineering, 20(3), 1984, 515-522.
[22] Liu, Y. J.; Rudolphi, T. J.: New identities for fundamental solutions and their applications to non-singular boundary element formulation, Computational mechanics, 24(4), 1999, 286-292.